Reinvestigating the Photoprotection Properties of a Mycosporine Amino Acid Motif

Abigail L. Whittock [1,2], Matthew A. P. Turner [2,3,4], Daniel J. L. Coxon [2,4,5], Jack M. Woolley [2], Michael D. Horbury [6] and Vasilios G. Stavros [2]*

[1] Analytical Science Centre for Doctoral Training, Senate House, University of Warwick, Coventry, United Kingdom, [2] Department of Chemistry, University of Warwick, Coventry, United Kingdom, [3] Molecular Analytical Science Centre for Doctoral Training, Senate House, University of Warwick, Coventry, United Kingdom, [4] Department of Physics, University of Warwick, Coventry, United Kingdom, [5] Diamond Science and Technology Centre for Doctoral Training, University of Warwick, Coventry, United Kingdom, [6] School of Electronic and Electrical Engineering, University of Leeds, Leeds, United Kingdom

With the growing concern regarding commercially available ultraviolet (UV) filters damaging the environment, there is an urgent need to discover new UV filters. A family of molecules called mycosporines and mycosporine-like amino acids (referred to as MAAs collectively) are synthesized by cyanobacteria, fungi and algae and act as the natural UV filters for these organisms. Mycosporines are formed of a cyclohexenone core structure while mycosporine-like amino acids are formed of a cyclohexenimine core structure. To better understand the photoprotection properties of MAAs, we implement a bottom-up approach by first studying a simple analog of an MAA, 3-aminocyclohex-2-en-1-one (**ACyO**). Previous experimental studies on **ACyO** using transient electronic absorption spectroscopy (TEAS) suggest that upon photoexcitation, **ACyO** becomes trapped in the minimum of an S_1 state, which persists for extended time delays (>2.5 ns). However, these studies were unable to establish the extent of electronic ground state recovery of **ACyO** within 2.5 ns due to experimental constraints. In the present studies, we have implemented transient vibrational absorption spectroscopy (as well as complementary TEAS) with Fourier transform infrared spectroscopy and density functional theory to establish the extent of electronic ground state recovery of **ACyO** within this time window. We show that by 1.8 ns, there is >75% electronic ground state recovery of **ACyO**, with the remaining percentage likely persisting in the electronic excited state. Long-term irradiation studies on **ACyO** have shown that a small percentage degrades after 2 h of irradiation, plausibly due to some of the aforementioned trapped **ACyO** going on to form a photoproduct. Collectively, these studies imply that a base building block of MAAs already displays characteristics of an effective UV filter.

Keywords: photoprotection, photostability, ultrafast, spectroscopy, mycosporine

INTRODUCTION

Ultraviolet (UV) radiation, in particular UVA (315–400 nm) and UVB (280–315 nm), that reaches the Earth's surface has both positive and negative effects on living organisms (Holick, 2004; Lucas et al., 2006; Humble, 2010). Consequently, nature has developed its own photoprotection to safeguard from harmful DNA damage. In humans, this natural photoprotection is achieved by producing melanin pigments that can absorb UVA and UVB radiation before it reaches DNA (Kollias et al., 1991). However, as melanin production is a delayed process and does not absorb all UVA and UVB radiation that reaches the skin, a more immediate form of protection is required, i.e., sunscreens (Eller and Gilchrest, 2000; Brenner and Hearing, 2008; Wang and Lim, 2016). Some UV filters found in sunscreens have been linked to the cause of damaging environmental effects as well as adverse dermatological effects (Bryden et al., 2006; Danovaro et al., 2008; Downs et al., 2013, 2016; Warshaw et al., 2013; Schaap and Slijkerman, 2018). As a result, there is an increased need for the identification of new UV filters that are less harmful to both the environment and humans. Drawing inspiration from nature offers a promising solution to these negative impacts. One approach is to base candidate UV filters off structures observed in plants and microorganisms (Bandaranayake, 1998; Dean et al., 2014; Baker et al., 2016, 2018; Horbury et al., 2017, 2018, 2019; Luo et al., 2017; Zhao et al., 2019a,b).
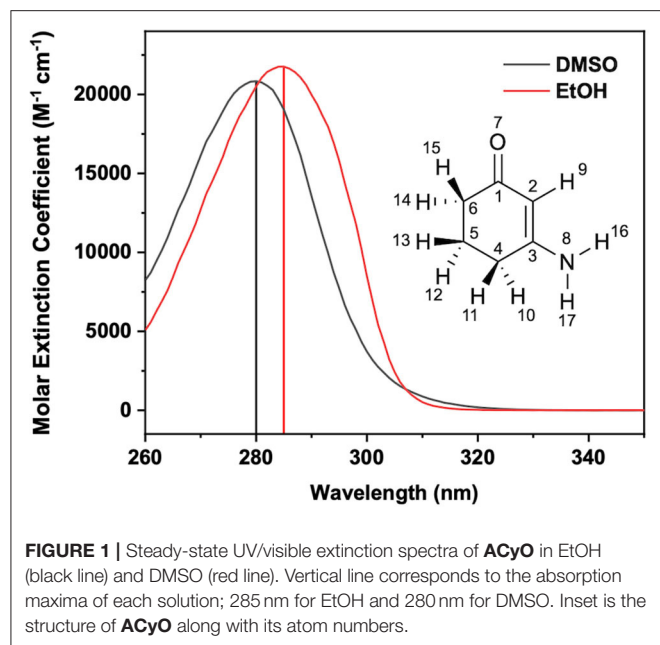
Cyanobacteria, fungi, macro- and microalgae all synthesize a family of molecules termed mycosporines and mycosporine-like amino acids (Sinha et al., 2007; Balskus and Walsh, 2010). In the literature, mycosporines and mycosporine-like amino acids are used synonymously. However, mycosporines are a family of molecules comprised of a cyclohexenone core and mycosporine-like amino acids are comprised of a cyclohexenimine core (herein both mycosporines and mycosporine-like amino acids will be termed MAAs) (Gao and Garcia-Pichel, 2011). MAAs present a strong absorbance band in the UVA and UVB, and their high photostability makes them highly desirable as potential UV filters (Bandaranayake, 1998; Conde et al., 2000, 2007; Sinha et al., 2000; Moliné et al., 2011; Rastogi and Incharoensakdi, 2014). As the extraction from natural sources and the synthetic preparation of natural MAAs produces small quantities, some work has been carried out on synthetic MAA motifs as an alternative; these molecules have also demonstrated promising levels of photostability thus far (White et al., 1989, 1995; Bandaranayake, 1998; Losantos et al., 2017, 2019; Woolley et al., 2018). Complementary studies, implementing computational and ultrafast spectroscopic techniques have been conducted on various MAA motifs in an effort to guide future UV filter design through knowledge of the photoprotection mechanisms

(Losantos et al., 2017, 2019; Woolley et al., 2018). Their finding will be briefly outlined here.

Losantos et al. (2017) implemented a CASPT2/CASSCF methodology to evaluate the minimum energy paths of a selection of MAA motifs composed of either a cyclohexenone or a cyclohexenimine core. Their results showed that a cyclohexenone core is potentially a poor scaffold for sunscreen applications, as following photoexcitation to the lowest optically bright S_2 excited state, a geometric distortion to a non-planar geometry leads to relaxation to the S_1 state via a S_2/S_1 conical intersection (CI). The electronic excited state population then traverses along the potential energy surface of the S_1, before becoming trapped in a minimum on the S_1 potential energy surface. For the cyclohexenimine core, Losantos et al. (2017) proposed that after initial photoexcitation to the lowest optically bright S_1 excited state, fast relaxation along an out-of-plane geometry distortion leads to an accessible S_1/S_0 CI, resulting in efficient repopulation of the electronic ground state. These results by Losantos et al. (2017) are corroborated by computational studies on the natural MAAs palythine and porphyra-334 (Sampedro, 2011; Koizumi et al., 2017; Hatakeyama et al., 2019). Interestingly, a computational study on gadusol (a molecule closely related to MAAs with a cyclohexenone core) found an accessible barrierless S_1/S_0 CI (Losantos et al., 2015). This, in addition to experimental studies on gadusol which reported high levels of photostability and rapid non-radiative decay as the dominant relaxation pathway (Arbeloa et al., 2011), indicates that molecules with a cyclohexenone core do display a number of ideal properties of a UV filter. Therefore, there is still much to learn about these cyclohexenone systems.

Woolley et al. (2018) and Losantos et al. (2019) have conducted transient electronic absorption spectroscopy (TEAS) experiments on MAA motifs to unravel their photoprotection mechanisms. Woolley et al. (2018) investigated two MAA motifs, the one of interest for this paper being 3-aminocyclohex-2-en-1-one (**ACyO**), see inset of **Figure 1** for the structure of **ACyO**. Their TEAS experimental results for **ACyO** in methanol (polar protic) and acetonitrile (polar aprotic) demonstrated a persistent excited state absorption (ESA), >2.5 ns, corroborating calculations from Losantos et al. (2017) that (at least a fraction of) **ACyO** becomes trapped in a minimum of the S_1. We note here that the calculated barrier to the S_1/S_0 CI is 0.04 eV for **ACyO** in the gas-phase (Woolley et al., 2018). Whilst population persisted in the excited state for nanoseconds, no real indication as to the percentage of **ACyO** that remained in the electronic excited state can be inferred from the TEAS experiment. This is due to TEAS experimental limitations as Woolley et al. (2018) were unable to observe a ground state bleach (GSB) of **ACyO**. Consequently, they could not establish the extent of electronic ground state recovery which would give a direct measure of the photostability of **ACyO**. Herein, we propose that UV pump infrared probe transient vibrational absorption spectroscopy (TVAS) can be used to measure the extent of vibrational ground state recovery in the electronic ground state on ultrafast timescales after photoexcitation, thus providing insight into the overall electronic ground state recovery of **ACyO**.

Abbreviations: UV, ultraviolet; MAA, mycosporine-like amino acid; ACyO, 3-aminocyclohex-2-en-1-one; TEAS, transient electronic absorption spectroscopy; CI, conical intersection; ESA, excited state absorption; GSB, ground state bleach; TVAS, transient vibrational absorption spectroscopy; DFT, density functional theory; EtOH, ethanol; DMSO, dimethyl sulfoxide; TDDFT, time-dependent density functional theory; FTIR, Fourier transform infrared; TEA, transient electronic absorption; MCT, mercury cadmium telluride; TVA, transient vibrational absorption.

FIGURE 1 | Steady-state UV/visible extinction spectra of **ACyO** in EtOH (black line) and DMSO (red line). Vertical line corresponds to the absorption maxima of each solution; 285 nm for EtOH and 280 nm for DMSO. Inset is the structure of **ACyO** along with its atom numbers.

To better understand the behavior of MAA motifs with a cyclohexenone core, we have performed TVAS, along with complementary TEAS and long-term irradiation studies on **ACyO**, to study the GSB recovery of its vibrational modes. We build on a study by Sui et al. (2012) who used density functional theory (DFT) to assign the vibrational modes of **ACyO** in acetonitrile and water; for reasons that will become apparent later, our experiments utilized ethanol (EtOH) and dimethyl sulfoxide (DMSO) as solvents. In order to assign the vibrational modes both in the electronic ground and excited state in EtOH and DMSO, we have implemented implicit- and explicit-solvent DFT and time-dependent DFT (TDDFT) (Casida, 1995) calculations using a similar level of theory to Sui et al. (2012). These high-level calculations were necessary for the identification of any overlapping electronic ground and excited state frequencies that would influence the interpretation of our TVAS data. We report in the present work that TVAS is a powerful technique that can extract GSB recovery quantum yields for the vibrational modes of a molecule on ultrafast timescales by comparing the extent of the bleach recovery with respect to the initial GSB. Previous publications have reported GSB recovery quantum yields, and how such qualitative information provides valuable insight into the efficiency of relaxation pathways (Holm et al., 2003; Rini et al., 2003; Murdock et al., 2014, 2015). For **ACyO**, the resultant quantum yields in addition to its overall photostability demonstrates promising properties that are required of a UV filter, providing some evidence for the photoprotective capabilities of MAAs with a cyclohexenone core.

MATERIALS AND METHODS

ACyO was purchased from Alfa Aesar (95% purity) and solutions of ∼40 μM, 4 mM, and 50 mM concentrations were made up

in the two solvents used in this study. EtOH (≥99.8%) and DMSO (≥99.9%) were purchased from VWR Chemicals and Fisher Scientific, respectively.

Steady-State Spectroscopy

ACyO samples in EtOH and DMSO of concentrations ∼40 μM contained in a 1 cm path length quartz cuvette were irradiated within a solar simulator (91,191–1,000, Oriel Instruments) which has an output power equivalent to the sun at the Earth's surface (∼1,000 W/m^2) for 7,200 s (120 min, 2 h). At various time intervals, UV/visible spectra were recorded using a UV/visible spectrometer (Cary 60, Agilent Technologies). To confirm that the degradation occurring was due to photodegradation, UV/visible spectra of **ACyO** solutions that had not been irradiated were taken before and after 7,200 s.

Fourier transform infrared (FTIR) spectra were obtained using a FTIR spectrometer (VERTEX 70v, Bruker) under a nitrogen environment to remove vibrational modes associated with atmospheric gases. 50 mM **ACyO** solutions in EtOH and DMSO were contained within a demountable liquid cell (Harrick Scientific Products Inc.) with a path length of 100 μm achieved by inserting 100 μm PTFE spacers between two CaF$_2$ windows (front window 1 mm and back window 2 mm thickness). The FTIR spectra were recorded over an energy range of 500–4,000 cm^{-1} with a resolution of 1 cm^{-1}.

Ultrafast Spectroscopy

TEAS and TVAS measurements were taken at the Warwick Center for Ultrafast Spectroscopy (WCUS: www.go.warwick.ac.uk/fac/sci/wcus). The setup of the TEAS experiment has been previously reported (Woolley et al., 2018), but it will be briefly described here. 4 mM solutions of **ACyO** in EtOH and DMSO were circulated through a demountable liquid cell with a path length of 100 μm set up in the same way as for FTIR spectroscopy described above. The samples were continuously circulated through the cell using a diaphragm pump (SIMDOS 02) to ensure a fresh sample was interacting with each laser shot. 800 nm pulses (12 W, 1 kHz, 40 fs) were generated by a Ti:Sapphire regenerative amplified laser system (Dual Ascend Pumped Spitfire Ace, Spectra-Physics) seeded by a Mai Tai (Spectra-Physics). The beam was split into four fractions, each fraction having its own recompression grating. One of the four fractions (3.5 W) was split into two further fractions in order to generate the pump and probe beams required for the TEAS experiments.

The first of the fractions (2.5 W) seeds an optical parametric amplifier (Topas-Prime with UV-extension, Light Conversion) which allows for a tuneable pump beam wavelength that includes 285 and 280 nm for photoexciting **ACyO** in EtOH and DMSO, respectively. These wavelengths were chosen as they correspond to the absorption maximum of each **ACyO** solution as displayed in **Figure 1**. The pump beam was set to a power of ∼500 μW and was focused beyond the sample holder to give a beam diameter of 500 μm at the sample holder. The probe beam was generated by focussing 5% of the remaining 1 W fundamental 800 nm beam which had been further attenuated and irised on to a vertically translated CaF$_2$ window (2 mm thickness) to

generate a white light continuum (320–720 nm). The probe pulse polarization was held at the magic angle (54.7°) with regards to the pump pulse polarization; this is done to avoid dynamical contributions from molecular reorientations. The path length of the 800 nm beam used to generate the probe beam can be varied to give pump-probe time delays (Δt) of −1 ps to 2.5 ns using a gold retroreflector mounted on a motorized optical delay line. Before reaching the sample, the pump beam passes through an optical chopper operating at a repetition rate of 500 Hz, blocking every other pulse of the 1 kHz pulse train. This allows for direct comparison of the signal detected by a fiber-coupled spectrometer (AvaSpec-ULS1650F, Avantes) for the pumped and unpumped samples which is displayed as changes in optical density (ΔOD) in the resultant transient electronic absorption (TEA) spectra.

Pump power dependency studies were carried out to ensure that ΔOD was linearly dependent on photon flux (see **Supplementary Figure 1**). Chirp correction of the TEA spectra was achieved using the KOALA package (Grubb et al., 2014). Global fitting of the TEA spectra was employed using the software package Glotaran (Mullen and Van Stokkum, 2007; Snellenburg et al., 2012), and a sequential kinetic model ($A \xrightarrow{\tau_{e1}} B \xrightarrow{\tau_{e2}} C \ldots$) was used over the entire spectral region of our probe (320–720 nm). The evolution associated difference spectra for the time constants of each fit can be found in **Supplementary Figure 2**. The quality of the fits was assessed through the associated residuals, see **Supplementary Figure 2**. The instrument response function, accounting for the temporal resolution of our TEAS measurements, was determined by fitting a Gaussian over the time zero artifacts of solvent-only scans and taking the full width half-maximum, see **Supplementary Figure 3** for the instrument response functions of EtOH and DMSO.

For the TVAS set up, 50 mM **ACyO** solutions in EtOH and DMSO were circulated through a demountable liquid cell the same way as reported above for the TEAS set-up. The pump beam was set to a higher power of 700 μW for the TVAS experiments. The probe beam (240 μW, 360 μm beam diameter) for the TVAS experiment was generated by seeding a second optical parametric amplifier (Topas-C, Spectra-Physics) with a second 3.5 W fraction of the fundamental 800 nm beam. The generated probe beam allows for a tuneable IR wavelength that includes 6,420 and 6,289 nm which were the wavelengths used in this experiment for **ACyO** in EtOH and DMSO, respectively. The path length of the probe beam was varied in a similar way to the TEAS set-up to give Δt of −1 ps to 1.8 ns. Atmospheric absorption lines were excluded by purging the probe line with nitrogen gas. Before the probe beam arrived at the sample compartment, it was incident on a CaF_2 beamsplitter where it was split equally in to reference and probe pulses. The reference pulse did not traverse the sample and was detected for the subtraction of shot-to-shot laser noise. The probe pulse passed through the sample where it was partially absorbed before entering an imaging spectrometer (iHR320, HORIBA Scientific). Once in the spectrometer, the probe was dispersed by a diffraction grating (6 μm blaze, 100 lines mm^{-1} resolution) onto a mercury cadmium telluride (MCT) detector array (FPAS-0144, Infrared

Systems Development) which was made up of two 64-pixel linear arrays—one each for the probe and reference pulses. The MCT detector was cooled using liquid nitrogen to eliminate thermal contributions to the signal. Like in the TEAS experiment, the pump beam passes through an optical chopper operating at a repetition rate of 500 Hz, blocking every other pulse of the 1 kHz pulse train. This allows for direct comparison of the signal for the pumped and unpumped samples which is displayed as ΔOD in the resultant transient vibrational absorption (TVA) spectra.

We converted between pixel number and wavelength using a mid-IR polystyrene calibration card (Perkin Elmer) as our reference. Similarly to the TEAS, pump power dependency studies were carried out, see **Supplementary Figure 4**. Only ~100 cm^{-1} windows were investigated for each solvent environment; this was dictated by the spectral congestion emanating from the solvent and the transition intensity of **ACyO** vibrational modes. Exponential fits of the GSB features were employed to extract time constants associated with the dynamical processes **ACyO** undergoes upon photoexcitation.

Computational Methods

Vibrational frequencies in the electronic ground (S_0) and excited (S_1) state were predicted for **ACyO** in both implicit- and explicit-solvent environments for EtOH and DMSO. The NWChem package (Valiev et al., 2010) was used to perform DFT and TDDFT calculations. These were done at the PBE0/cc-pVTZ level of theory (Davidson, 1996; Perdew et al., 1996; Adamo and Barone, 1999). Implicit-solvent calculations were employed using the COSMO solvent model for both EtOH and DMSO which models each solvent's dielectric parameters (Klamt and Schüürmann, 1993; Winget et al., 1999; York and Karplus, 1999). We add that the level of theory described has previously been used for a similar system studied by Turner et al. (2019) which also performed vibrational frequency calculations. Due to discrepancies in the calculated S_0 vibrational frequencies and their corresponding vibrational modes, in addition to the fact EtOH and DMSO interact strongly with **ACyO**, it was determined that explicit-solvent contributions should be considered. See **Supplementary Table 1** and **Supplementary Figure 5** for implicit-solvent vibrational frequency results. This high-level of theory has been used so that accurate electronic excited state frequencies are predicted, which in turn provides valuable insight into any overlapping electronic ground and excited state frequencies in the TVAS probe region. As a result, reliable GSB recovery quantum yields can be extracted from the TVA spectra. Although neither implicit- or explicit-solvent results are perfect, the scaling factors required for explicit-solvent (0.997 and 0.982 for EtOH and DMSO, respectively) were significantly closer to 1 than implicit-solvent (0.976 for both solvents) indicating improved accuracy for the explicit-solvent calculations. Therefore, the decision was made to report explicit-solvent herein. Further to this, the asymmetry of the 1.8 ns lineout from our TVA spectra can be explained by the computed S_1 frequencies determined by EtOH explicit-solvent (see later discussion). On the other hand, the computed S_1 frequencies for EtOH implicit-solvent do not provide such clarity. Furthermore, regardless of whether an

implicit- or explicit-solvent model is used for **ACyO** in DMSO, there are no overlapping S_1 frequencies with the probed peaks in the TVAS experiment.

Solvent shells were generated through a similar method used by Zuehlsdorff et al. (2017) and Turner et al. (2019). In this, a classical molecular dynamics simulation was performed using the AMBER package (Case et al., 2015). **ACyO**, optimized in DFT at the level of theory discussed previously, was immersed in a 20 Å cube of explicit-solvent (both EtOH and DMSO). The system was heated over 20 ps in the NVT ensemble wherein the temperature is raised from 0 to 300 K. This, along with all further calculations, was achieved using a Langevin thermostat with a collision frequency of 1 ps^{-1}. Following this, a 400 ps pressure equilibration is utilized in the NPT isothermic-isobaric ensemble with the pressure fixed at 1 atm. Next, the system was equilibrated at a constant temperature of 300 K for 100 ps. Finally, snapshots were generated via a further NVT ensemble run, this time with a fixed temperature of 300 K for 8 ns. 2000 snapshots were extracted by recording a frame every 4 ps. By saving every tenth snapshot, 200 of these snapshots were exported. Within each snapshot, the solute and hydrogen bonding solvent molecules were extracted by removing any solvent molecules that were further than 1.5 Å from the solute.

As has been previously conducted by Turner et al. (2019), four snapshots were chosen for each solvent. Each snapshot has a different solvent environment and initial structures are shown in **Supplementary Table 2**. In the case of DMSO, only two solvent molecules were within 1.5 Å of **ACyO** and hence the four chosen snapshots were selected to ensure that the DMSO molecules were in different orientations in each snapshot (see **Supplementary Table 2**). For EtOH, a variety of solvent environments over the 200 snapshots were found, the most common being; one EtOH on the carbonyl oxygen and one EtOH on the amine hydrogen, two EtOH on the carbonyl oxygen and one EtOH on the amine hydrogen, one EtOH on the carbonyl oxygen and two EtOH on the amine hydrogens and finally two EtOH on the carbonyl oxygen and two EtOH on the amine hydrogens. One of each environment was selected for the calculations in order to evaluate the different solvent environments determined by molecular dynamics (see **Supplementary Table 2**). Calculations of full solvent shells were not conducted for the present work. This is due to previous findings by Turner et al. (2019) who found that full solvent shell calculations and smaller clusters with only two solvent molecules did not generate notable differences in the calculated vibrational frequencies. Furthermore, such calculations take significant computational expenditure due to the larger number of atoms.
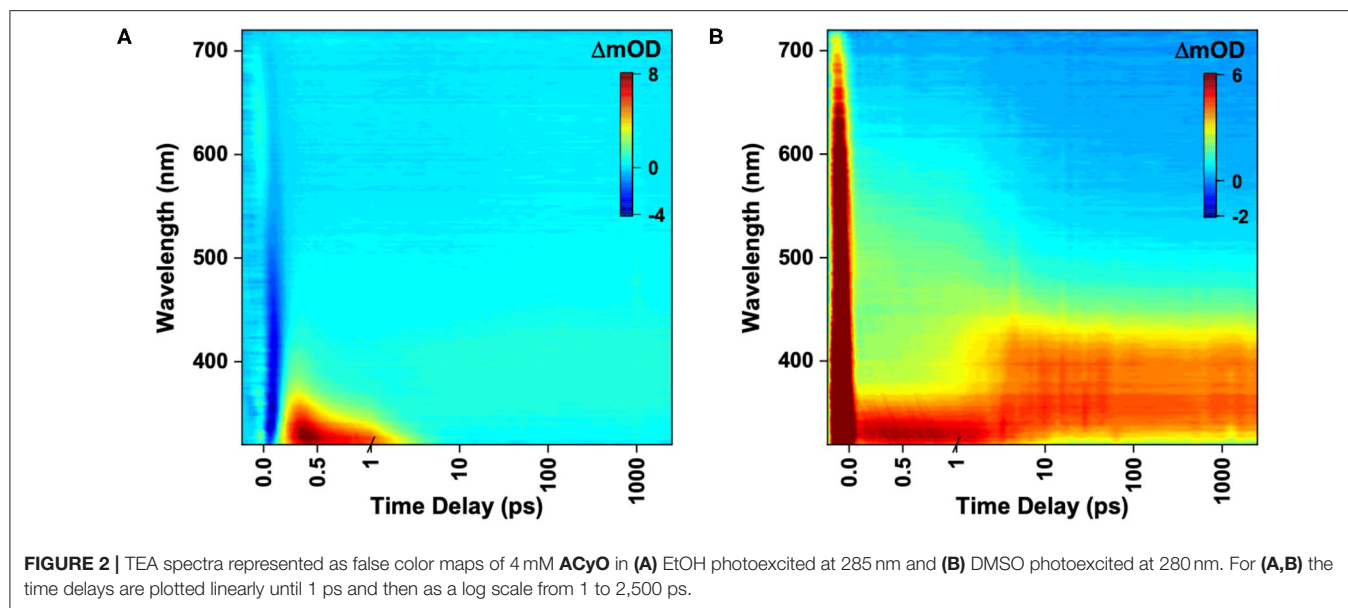
The DFT calculations that were conducted were as follows: initially a geometry optimisation was employed on all the implicit- and explicit-solvent structures stated above followed by an electronic ground state frequency calculation. Vertical excitations were conducted and the results corroborated previous work stating that the first optically bright state is the S_2 (Sui et al., 2012; Losantos et al., 2017). Following this calculation, electronic excited state geometry relaxation calculations were carried out to determine the relaxed geometry on the S_1 excited state. The S_1 was chosen based on previous work that computed the minimum energy path and found that **ACyO** becomes trapped in the minimum of its S_1 excited state (Losantos et al., 2017; Woolley et al., 2018). Finally, electronic excited state vibrational frequency calculations were conducted on the S_1 relaxed geometry. Only averaged explicit-solvent vibrational frequencies for **ACyO** in EtOH and DMSO are presented herein, but all individual results for the implicit- and explicit-solvent environments can be found in the Supplementary Material including the optimised geometries and vertical excitation results (see **Supplementary Tables 1–5**). We also note that all reported frequencies are between 1,500 and 1,750 cm^{-1} as it is the region of interest for the present work and extensive evaluation of the computed frequencies is outside the scope of this work.

Scaling factors were applied to the calculated S_0 and S_1 frequencies and were calculated by using one experimental peak as a reference so that the calculated frequency exactly matches the reference experimental peak. This method is common practice and has been employed in a similar study by Turner et al. (2019) and Grieco et al. (2018). The chosen S_0 reference peaks were 1,559 and 1,577 cm^{-1} for **ACyO** in EtOH and DMSO, respectively, and were chosen because they were the strongest experimental peaks observed between 1,500 and 1,750 cm^{-1}. As there were no clear experimental S_1 frequencies obtained in this study, we tentatively applied the same scaling factor to the S_1 frequency calculation as was applied to the S_0 frequency calculation for both solvent environments; a similar approach was implemented by Baker et al. (2015). The resultant scaling factors for the averaged explicit-solvents snapshots of **ACyO** in EtOH and DMSO were 0.997 and 0.982, respectively.

RESULTS AND DISCUSSION

We first take a look at the TEA spectra acquired for **ACyO** in EtOH and DMSO which are displayed as false color maps in **Figure 2**; for lineouts of the TEA spectra see **Supplementary Figure 6**. The choice to use EtOH and DMSO as solvents was firstly to demonstrate dynamics in different solvent types (protic and aprotic), and secondly because these solvents displayed clear spectral windows in the region of interest for our FTIR and TVAS experiments. We note here that our TEA spectra strongly correlate with the findings of Woolley et al. (2018); the **ACyO** excited-state dynamics in EtOH are very similar to those observed in methanol (as might be expected; both polar and protic), and the **ACyO** excited state dynamics in DMSO are also very similar to those observed in acetonitrile (both polar and aprotic). Hence only a brief discussion is required here. Starting with **ACyO** in EtOH shown in **Figure 2A**, we observe a negative feature at early pump-probe time delays ($\Delta t < 0.2$ ps) identified as multiphoton initiated dynamics (see **Supplementary Figure 1**), followed by an intense ESA centered at ∼330 nm which blue-shifts out of the probe window and mostly decays by ∼5 ps. A second ESA of less intensity grows in within 5 ps centered at ∼400 nm and persists to the final time delay of our experiment ($\Delta t = 2.5$ ns), see **Supplementary Figure 6A** for lineouts. We now take a look at

FIGURE 2 | TEA spectra represented as false color maps of 4 mM **ACyO** in **(A)** EtOH photoexcited at 285 nm and **(B)** DMSO photoexcited at 280 nm. For **(A,B)** the time delays are plotted linearly until 1 ps and then as a log scale from 1 to 2,500 ps.

the TEA spectra for **ACyO** in DMSO shown in **Figure 2B**. At early time delays, there is a broad ESA spanning from 320 to 720 nm peaking at ∼330 nm. The broad ESA narrows and the greatest intensity red-shifts to center at ∼370 nm in around 5 ps. This feature then persists to the maximum Δt of the experiment ($\Delta t = 2.5$ ns), see **Supplementary Figure 6B** for lineouts.

Although mentioned previously, it is worth revisiting the proposed cyclohexenone core deactivation pathway upon photoexcitation reported by Losantos et al. (2017) as it is the basis for the time constant assignment presented herein. The vertical excitation calculations that were carried out for the present study corroborate previous work which states that **ACyO** is initially photoexcited to the S_2 through a $\pi_L^* \leftarrow \pi_H$ transition (see **Supplementary Table 4** and **Supplementary Figure 7**) (Sui et al., 2012; Losantos et al., 2017). The computed minimum energy path demonstrates that a similar molecule to **ACyO** (NHCH$_3$ substituent on C_3, herein termed the NHCH$_3$ molecule, see inset of **Figure 1**) studied by Losantos et al. (2017) redistributes its energy after photoexcitation causing a geometric distortion. This leads to an accessible S_2/S_1 CI where it then vibrationally cools to a minimum on the S_1. Woolley et al. (2018) conducted complementary calculations on **ACyO** finding that the calculated energy barrier to the S_1/S_0 CI for **ACyO** in the gas phase is 0.04 eV (Woolley et al., 2018), *cf.* 0.2 eV for the NHCH$_3$ molecule studied by Losantos et al. (2017). We now assign the dynamical processes to the extracted time constants from the global sequential fit, re-evaluating our previous work in light of the present and previous data.

Global fitting of **ACyO** in EtOH extracted three time constants and can be found in **Table 1**; we add that as the negative feature is the result of multiphoton initiated dynamics, it has been omitted from the global fit. We propose that the first time constant, $\tau_{e1} = 0.24$ ps, corresponds to the initial geometry relaxation and solvent rearrangement **ACyO** undergoes in order to traverse the S_2/S_1 CI and populate the S_1 potential energy

TABLE 1 | Time constants and associated errors extracted from the sequential global fit of the TEA spectra for **ACyO** in EtOH and DMSO.

Time constant	EtOH	DMSO
τ_{e1}	0.24 ± 0.035 ps	2.7 ± 0.038 ps
τ_{e2}	1.2 ± 0.035 ps	>2.5 ns
τ_{e3}	>2.5 ns	

surface. We attribute the second time constant, $\tau_{e2} = 1.2$ ps, with the vibrational cooling of **ACyO**, via vibrational energy transfer (both intramolecular and intermolecular), as it samples the S_1 potential energy surface before overcoming the barrier to, and traversing through the S_1/S_0 CI. From the evolution associated difference spectra and lineouts of **ACyO** in EtOH (see **Supplementary Figures 2A, 6A**), narrowing of the ESA is observed which is a good indication that vibrational cooling on the S_1 potential energy surface is occurring (also the case for **ACyO** in DMSO, see **Supplementary Figures 2B, 6B**). We note here that as the ESA (∼330 nm) decays out of the probe window in our TEA spectra, it is possible that τ_{e2} is an underestimation of the time constant associated with repopulation of the electronic ground state. The final time constant, $\tau_{e3} > 2.5$ ns, corresponds to any **ACyO** that has remained trapped in the minimum of the S_1 excited state.

The global fitting of **ACyO** in DMSO extracted two time constants, see **Table 1**. We have assigned the first time constant, $\tau_{e1} = 2.7$ ps, to a collection of processes; geometry relaxation and solvent rearrangement **ACyO** undergoes to reach the S_2/S_1 CI (similar to τ_{e1} for **ACyO** in EtOH), followed by vibrational energy transfer along the S_1 potential energy surface before repopulating the electronic ground state, mediated via the S_1/S_0 CI (similar to τ_{e2} for **ACyO** in EtOH). As with **ACyO** in EtOH, the second time constant, $\tau_{e2} > 2.5$ ns, corresponds to any **ACyO** that is still

populated in the S_1 excited state beyond the final time delay of our experiment. Based on the above assignments, we attribute the ESA at ~400 nm which grows in within ~5 ps and persists beyond the final time delay in the TEA spectra of both solvents (**Figures 2A,B**) to ESA from the S_1 minimum. For **ACyO** in DMSO, the ESA at extended time delays (2.5 ns) is still relatively large in intensity; however, from our TVA spectra we know that a large percentage of **ACyO** molecules have already returned to their electronic ground state within ~5 ps, see later discussion. Plausible explanations are that the strength of the ESA from the S_1 minimum is greater than at other locations along the potential energy surface, or the ESA at early time delays is dampened by a competing stimulated emission. Thus, a reduced population on the S_1 minimum could (and evidently does) result in a more intense ESA. Further to this, we have determined through our TVA spectra that the relaxation mechanism in both solvents is the same, however, there is evidently a solvent dependence on the strength of the ESAs from different positions on the relaxation pathway. For example, the strength of the ESA from the S_1 minimum in EtOH is evidently weaker than the strength of the ESA from the S_1 minimum in DMSO. This highlights the influence of solvent on the oscillator strength, which was previously discussed by Woolley et al. (2018). Furthermore, our assignment here (and below) of population trapped on S_1 concurs with previous work in that there is a barrier to the S_1/S_0 CI (Losantos et al., 2017; Woolley et al., 2018).

However, we highlight again that no indication on the percentage of **ACyO** trapped in the S_1 excited state can be inferred from the TEA spectra. To glean further insight into this, we conducted both TVAS and steady-state irradiation studies. To begin the TVAS discussion, we must first look at the FTIR spectra of **ACyO** in EtOH and DMSO and assign the vibrational modes to the peaks of interest. **Table 2** gives the averaged explicit-solvent calculated S_0 frequencies (with associated scaling factors of 0.997 and 0.982 for EtOH and DMSO, respectively) and associated vibrational modes. **Figure 3** is a visual representation of the calculated frequencies overlaying the FTIR spectra for each **ACyO** solution between 1,500 and 1,750 cm^{-1}. Only this region of the FTIR spectra is displayed as it is the region that is not

masked by solvent absorption and includes the strongest peaks. The relative strengths of the vibrations have also been scaled to match the reference peaks at 1,559 and 1,577 cm^{-1} for **ACyO** in EtOH and DMSO, respectively.

The FTIR spectra for **ACyO** in EtOH and DMSO have many differences such as: peak positions; peak widths; peak intensities; and, to a lesser extent, assigned vibrational modes. This highlights how solvent environment effects the observed FTIR spectra and provides a further justification for our choice to implement explicit-solvent calculations. Similarities between the two spectra are that the strongest peak in each spectrum corresponds to the $C_2=C_3$ stretch (given in **Table 2** are the additional vibrational modes for this peak in each solvent but for simplicity it is referred to as the $C_2=C_3$ stretch herein) and the weaker peaks at highest wavenumbers in the presented spectra in **Figure 3** correspond to the H_{16}-N_8-H_{17} scissor mode, see inset of **Figure 1** for atom numbers. A similar pattern was observed in a previous study which computed the vibrational frequencies for **ACyO** in water and acetonitrile adding further credence to our assignment (Sui et al., 2012).

Generally, the calculated peak positions are in good agreement with the experimental data with the largest error being <20 cm^{-1} for the majority of the calculated frequencies. The only exception to this is the calculated frequency of 1,647 cm^{-1} for **ACyO** in DMSO which is shifted ~45 cm^{-1} to a higher wavenumber compared to the experimental peak. This could be explained by the fact we only consider two DMSO molecules interacting with **ACyO** in our calculations compared to a full solvation shell interaction between solute and solvent. However, due to the reasonable accuracy for all other frequencies and because this vibrational mode does not have a corresponding S_1 frequency (see later discussion), the computational expenditure required for a full solvent shell calculation is deemed unnecessary.

The TVA spectra for **ACyO** in EtOH and DMSO and their associated tri-exponential fits for the GSB are shown in **Figure 4**. Global fitting was not implemented here as we were only interested in the GSB recovery of the probed vibrational modes. Furthermore, we note that our tri-exponential fits begin at the GSB signal maximum; for **ACyO** in EtOH this was 0.4 ps, and

TABLE 2 | Computed S_0 and S_1 vibrational frequencies and their associated vibrational modes at the PBE0/cc-pVTZ level of theory for **ACyO** in EtOH and DMSO between 1,500 and 1,750 cm^{-1}.

Solvent	S_0 frequencies, cm^{-1} (Rel. strength)	Vibrational mode S_0	S_1 frequencies, cm^{-1} (Rel. strength)	Vibrational mode S_1
EtOH	1,559 (298)	$C_2=C_3$ stretch + $C_1=O_7$ stretch + C_2-H_9 bend	1,517 (12)	H_{10}-C_4-H_{11} scissor
	1,605 (4)	$C_2=C_3$ stretch + $C_1=O_7$ stretch + H_{16}-N_8-H_{17} scissor	1,565 (46)	$C_2=C_3$ stretch + H_{10}-C_4-H_{11} scissor + N_8-H_{17} bend + C_2-H_9 bend
	1,685 (27)	H_{16}-N_8-H_{17} scissor	1,714 (34)	H_{16}-N_8-H_{17} scissor
DMSO	1,577 (185)	$C_2=C_3$ stretch + C_4-H_{10} bend + N_8-H_{17} bend + C_2-H_9 bend	1,523 (91)	$C_2=C_3$ stretch + C_4-H_{10} bend + N_8-H_{17} bend + C_2-H_9 bend
	1,647 (111)	$C_1=O_7$ stretch + H_{16}-N_8-H_{17} scissor	No corresponding frequency	
	1,675 (9)	H_{16}-N_8-H_{17} scissor	1,645 (44)	H_{16}-N_8-H_{17} scissor

*The presented frequencies are an average of four explicit-solvent snapshots except for the S_1 EtOH frequencies which are an average of two explicit-solvent snapshots. Scaling factors of 0.997 and 0.982 were applied to the calculated frequencies for **ACyO** in EtOH and DMSO, respectively. See text for details.*
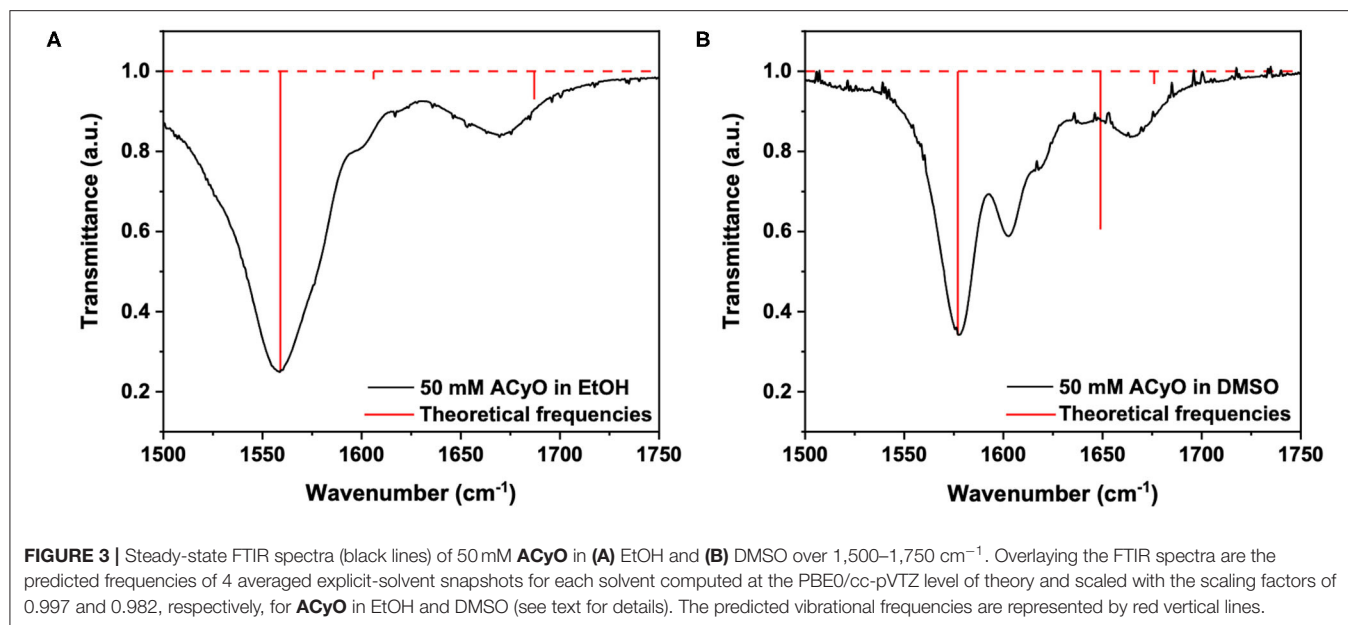
FIGURE 3 | Steady-state FTIR spectra (black lines) of 50 mM **ACyO** in **(A)** EtOH and **(B)** DMSO over 1,500–1,750 cm^{-1}. Overlaying the FTIR spectra are the predicted frequencies of 4 averaged explicit-solvent snapshots for each solvent computed at the PBE0/cc-pVTZ level of theory and scaled with the scaling factors of 0.997 and 0.982, respectively, for **ACyO** in EtOH and DMSO (see text for details). The predicted vibrational frequencies are represented by red vertical lines.

for **ACyO** in DMSO this was 0.7 ps. In fitting this way, we avoid any coherent artifacts that occur at early time delays such as perturbed free induction decay (Hamm, 1995). We start the TVAS discussion by first highlighting that in both solvents, full GSB recovery is not achieved at $\Delta t = 1.8$ ns. This is in accordance with the TEA spectra *supra* which show excited state dynamics persisting beyond $\Delta t = 2.5$ ns. The extracted GSB recovery quantum yields from the integrated signal of each GSB feature were calculated to be 86 and 76% for **ACyO** in EtOH (over 1,540–1,550 cm^{-1}, see later discussion for our choice to use this integration region) and DMSO (over 1,560–1,585 cm^{-1}) respectively. Greater GSB recovery is observed for **ACyO** in EtOH compared to **ACyO** in DMSO by 10%. A similar trend was observed for the long-term irradiation studies of **ACyO** presented below. The two are intuitively related and imply that more **ACyO** molecules in EtOH are able to overcome the barrier to access the S$_1$/S$_0$ CI within $\Delta t = 1.8$ ns. Therefore, there is less population trapped in the electronic excited state that can undergo pathways leading to photodegradation compared to **ACyO** in DMSO. We note here that the GSB recovery quantum yields we quote only consider GSB recovery that occurs within 1.8 ns, and it is possible that further electronic ground state repopulation may occur after that time.

The time constants extracted from the fit for **ACyO** in EtOH (1,559 cm^{-1} peak) and DMSO (1,577 cm^{-1} peak) are reported in **Table 3**. We begin by assigning the dynamical processes of the extracted time constants for **ACyO** in EtOH. The first time constant, $\tau_{v1} = 0.53$ ps, is on a similar timescale to τ_{e2} from the TEA spectra fit which would suggest that similar dynamics are occurring as we have reported; geometry relaxation and solvent rearrangement of **ACyO**, followed by vibrational energy transfer on S$_1$ and then repopulation of S$_0$. However, as TVAS only measures the GSB recovery of the fundamental vibration (being probed) in the electronic ground state, it provides little

information about the dynamics in the electronic excited state, making comparison between τ_{e2} and τ_{v1} tentative. As a result, we note that τ_{v1} may only be incorporating some of the electronic excited state dynamics and repopulation of the electronic ground state is most likely occurring on a longer time scale. The second time constant for the TVA spectra, $\tau_{v2} = 49$ ps, is associated with the vibrational cooling of the electronic ground state through vibrational energy transfer, both intramolecular and intermolecular (to solvent). This longer timescale can only be observed in the TVA spectra as the GSB of **ACyO** falls outside of the probe window for our TEAS experiment. As a result, no spectral signatures of vibrational cooling on the S$_0$ are present in the TEA spectra, and thus no time constant can be assigned to this photophysical process. Furthermore, we do not observe a blue-shifting of the transient vibrational bands with time that is often associated with the anharmonicity of vibrations (Nibbering et al., 2005), and instead observe a slight red-shift for **ACyO** in EtOH (**Figure 4A**). We reconcile this through the following: firstly, it is possible that the probed vibration is relatively harmonic; and secondly, the ESA from the S$_1$ minimum between ∼1,560 and 1,570 cm^{-1}, which contributes toward the GSB recovery and causes an asymmetric line shape at extended time delays (see later discussion), is likely the main cause of the apparent red-shift. For **ACyO** in DMSO (**Figure 4B**), neither a red-shift or a blue-shift is observed, providing confidence that the probed vibrations are relatively harmonic. The final time constant for **ACyO** in EtOH, $\tau_{v3} > 1.8$ ns, is due to the incomplete GSB recovery. Drawing reference to our TEAS data, this is very likely attributed to the long-lived **ACyO** trapped in the minimum of the S$_1$.

The calculated S$_1$ frequencies and associated vibrational modes for **ACyO** in EtOH can be found in **Table 2** and were scaled using the same scaling factor that was applied to the S$_0$ frequencies, 0.997. The reported frequencies are an average
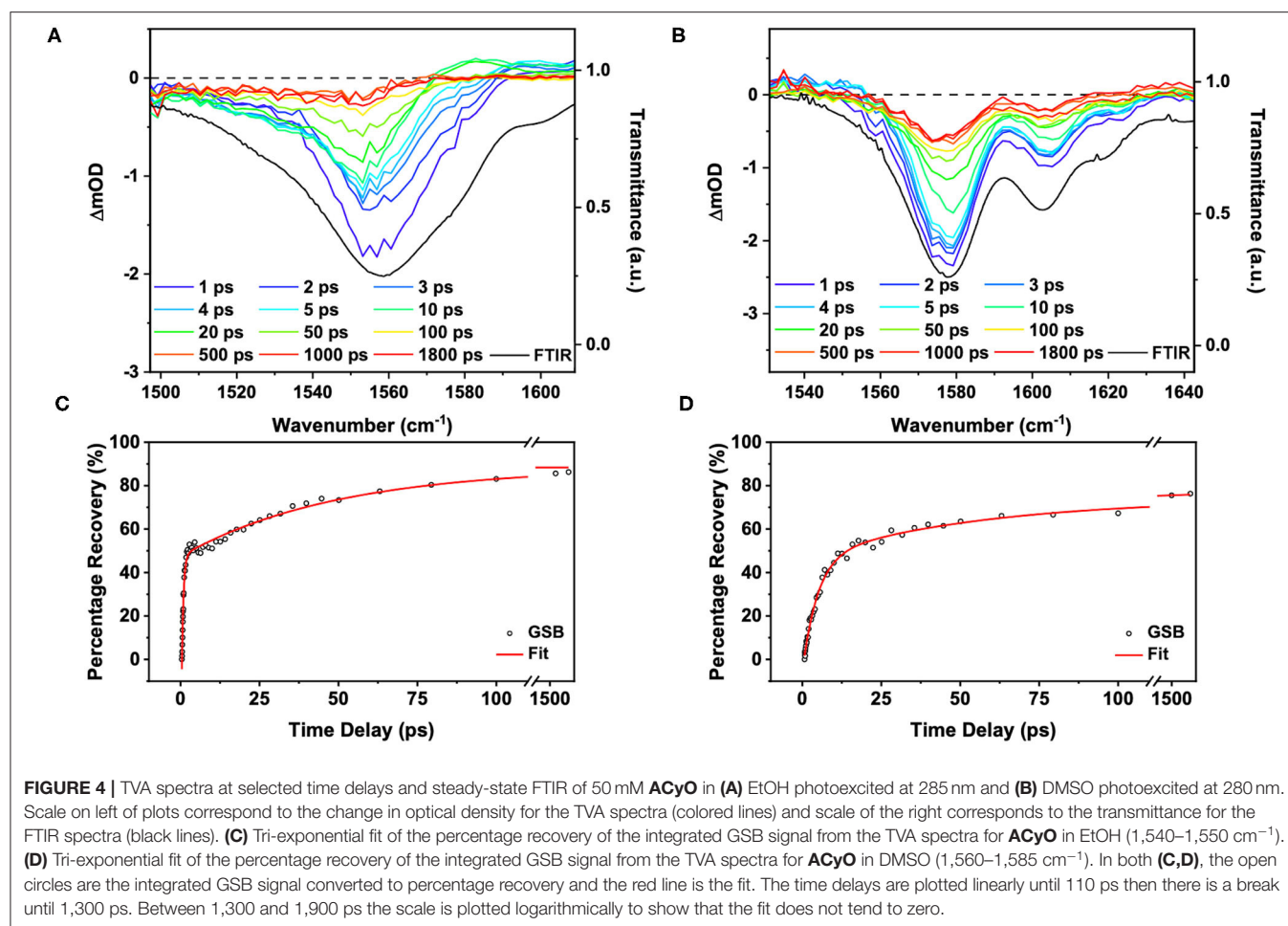
FIGURE 4 | TVA spectra at selected time delays and steady-state FTIR of 50 mM **ACyO** in **(A)** EtOH photoexcited at 285 nm and **(B)** DMSO photoexcited at 280 nm. Scale on left of plots correspond to the change in optical density for the TVA spectra (colored lines) and scale of the right corresponds to the transmittance for the FTIR spectra (black lines). **(C)** Tri-exponential fit of the percentage recovery of the integrated GSB signal from the TVA spectra for **ACyO** in EtOH (1,540–1,550 cm^{-1}). **(D)** Tri-exponential fit of the percentage recovery of the integrated GSB signal from the TVA spectra for **ACyO** in DMSO (1,560–1,585 cm^{-1}). In both **(C,D)**, the open circles are the integrated GSB signal converted to percentage recovery and the red line is the fit. The time delays are plotted linearly until 110 ps then there is a break until 1,300 ps. Between 1,300 and 1,900 ps the scale is plotted logarithmically to show that the fit does not tend to zero.

TABLE 3 | Time constants and associated errors extracted from the tri-exponential fit of the integrated GSB signal from the TVA spectra for **ACyO** in EtOH (1,540–1,550 cm^{-1}) and DMSO (1,560–1,585 cm^{-1}).

Time constant	EtOH (1,559 cm^{-1})	DMSO (1,577 cm^{-1})
τ_{v1}	0.53 ± 0.028 ps	4.7 ± 0.35 ps
τ_{v2}	49 ± 2.9 ps	55 ± 9.0 ps
τ_{v3}	>1.8 ns	>1.8 ns

of two snapshots due to difficulties experienced when running our EtOH explicit-solvent excited state calculations, see the **Supplementary Material** for more details. We draw confidence on the validity of these results from the similarity between the two snapshots, alongside the consistency of the results observed in DMSO. Future studies may invest further into converging more snapshots, but this has a high computational cost and is beyond the scope of the work. The only S$_1$ frequency which had a clear corresponding S$_0$ frequency between 1,500 and 1,750 cm^{-1} for **ACyO** in EtOH was for the H$_{16}$-N$_8$-H$_{17}$ scissor vibrational mode. This mode is shifted ~30 cm^{-1} in the S$_1$ to a higher wavenumber of 1,714 cm^{-1}. Additionally, two other excited state

frequencies were found during the calculation in the region of interest. These were computed as 1,517 and 1,565 cm^{-1} and they correspond to the H$_{10}$-C$_4$-H$_{11}$ scissor and the C$_2$=C$_3$ stretch (plus several other vibrational modes), respectively, see **Table 2** for full vibrational mode assignment. These vibrational modes are convoluted on top of the GSB of the C$_2$=C$_3$ stretch at 1559 cm^{-1} that we probed in the TVAS experiment. The relative strengths of the two S$_1$ frequencies are significantly smaller than the S$_0$ frequency therefore, we would expect any ESAs to be much weaker in intensity compared to the GSB. That being said, from the TVA spectra in **Figure 4**, a small ESA feature is observable at a wavenumber of ~1,570 cm^{-1} and above; present between 10–20 ps and decaying by 50 ps. We are unable to definitely pinpoint the origin of this feature. Possible suggestions include probing: (1) the C$_2$=C$_3$ stretch in S$_1$; and (2) a higher lying vibration in **ACyO** in the ground electronic state which subsequently cools. Indeed, the decay of this feature matches τ_{v2} adding credence to the latter assignment. Importantly, at 1.8 ns, the asymmetry of the GSB feature insinuates that an ESA is contributing toward the GSB recovery between ~1,560 and 1,570 cm^{-1}. This matches the computed S$_1$ frequency at 1,565 cm^{-1}, therefore, we assign it to the population of **ACyO** trapped in the S$_1$ minimum. The ESA does not emerge above baseline due to the fact the transition is six

times weaker than the probed electronic ground state transition, see **Table 2**. Due to the convolution of peaks, we highlight that for the GSB recovery quantum yield and fitting of the GSB, a smaller region (1,540–1,550 cm^{-1}) was integrated between to negate as many contributions from the overlapping ESAs as possible. We appreciate that there is still a possibility that the ESA is contributing to the GSB recovery, hence we report the GSB recovery quantum yield of 86% as being the upper limit in this case.

The TVA spectra of **ACyO** in DMSO is more straightforward to interpret due to no convoluted S_1 frequencies computed by TDDFT calculations. A tri-exponential fit of the integrated signal of the 1,577 cm^{-1} vibration (1,560–1,585 cm^{-1}) can be found in **Figure 4** and its corresponding time constants can be found in **Table 3**. The same assignment of the time constants is made for **ACyO** in DMSO as that reported above for **ACyO** in EtOH. τ_{v1} (4.7 ps) is assigned to the geometry relaxation and solvent rearrangement **ACyO** undergoes to access the S_2/S_1 CI, followed by vibrational cooling on the S_1 and traversing through the S_1/S_0 CI to repopulate the electronic ground state. Like in **ACyO** in EtOH, the timescales of τ_{e1} and τ_{v1} are similar. τ_{v2} (55 ps) is assigned to the vibrational cooling of **ACyO** on the S_0 through vibrational energy transfer. Again, comparison to the TEA spectra cannot be made for τ_{v2} due to TEAS experimental limitations as discussed above. The final time constant, $\tau_{v3} > 1.8$ ns, is assigned to any **ACyO** molecules trapped in the minimum of the S_1 potential energy surface.

We conclude the TVAS discussion by evaluating the S_1 vibrational frequency calculations for **ACyO** in DMSO which can be found in **Table 2**. These computed frequencies are an average of four explicit-solvent snapshots and were simpler to assign to their corresponding electronic ground state frequencies, unlike **ACyO** in EtOH. For the $C_2=C_3$ stretch vibration, calculated frequency values of 1,577 cm^{-1} in the S_0 state and 1,523 cm^{-1} in the S_1 state are reported in **Table 2**. For the H_{16}-N_8-H_{17} scissor vibration, the calculated frequency values are 1,675 cm^{-1} in the S_0 state and 1,645 cm^{-1} in the S_1 state. Therefore, upon $S_1 \leftarrow S_0$ excitation, the harmonic frequencies of both vibrations are shifted to a lower wavenumber; the frequency of the $C_2=C_3$ stretch vibration by ∼50 cm^{-1} and the frequency of the H_{16}-N_8-H_{17} scissor vibration by ∼30 cm^{-1}. There was no corresponding S_1 frequency for the $C_1=O_7$ stretch plus H_{16}-N_8-H_{17} scissor that was computed as 1,647 cm^{-1} in the electronic ground state. Additionally, there were no other new S_1 frequencies appearing between 1,500 and 1,750 cm^{-1} and this insinuates that no ESA features should be present in the TVA spectra, which is the case as seen in **Figure 4B**. As a result, we are confident that the GSB recovery quantum yield for **ACyO** in DMSO (76%) is a more accurate value than the GSB recovery quantum yield for **ACyO** in EtOH (86%). We add that a degenerate pump-probe experiment would complement the observed GSB recovery quantum yields obtained from our TVAS experiments; however, for the present study, the TVAS data provides a good starting point with which to progress with future studies.
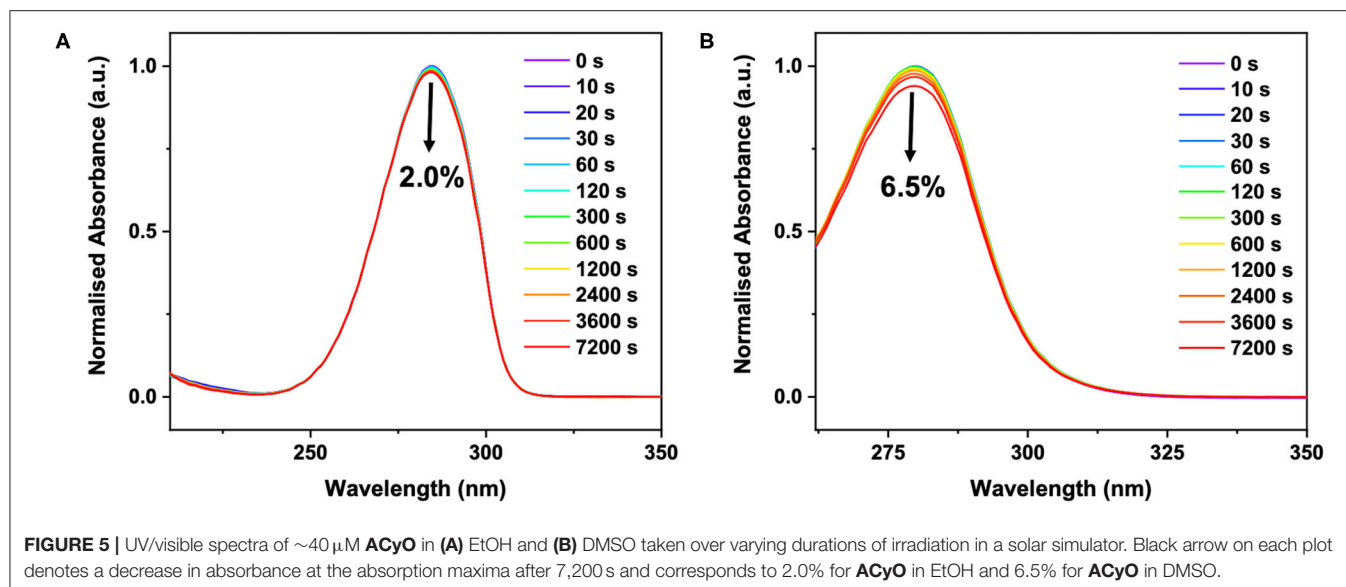
In our efforts to link our ultrafast dynamics studies of **ACyO** (and the GSB recovery quantum yields thereof) to the long-term photostability of **ACyO**, we performed long-term irradiation studies and the results are presented in **Figure 5**. The data shows that after 7,200 s, only 2.0 and 6.5% degradation of signal at the absorption maxima occurred for **ACyO** in EtOH and DMSO, respectively. Control measurements confirmed that all degradation observed was due to photodegradation, see **Supplementary Figure 8**. The impressive levels of photostability of **ACyO** in both solvents must stem from highly efficient repopulation of the electronic ground state as we observed in our TVAS studies *supra*. In the long-term irradiation study, we see no emergence of an absorbance at ∼400 nm in either solvent, eliminating the possibility that the long-lived feature in the TEA spectra is a photoproduct. This provides further support that the long-lived feature observed in our TEA and TVA spectra is **ACyO** population trapped in S_1 state. Losantos et al. (2017) predicted that the cyclohexenone unit they studied would radiatively decay after becoming trapped on the S_1 in order to repopulate the molecules' electronic ground state. However, in accordance with Woolley et al. (2018) we observed no radiative decay implying that **ACyO** must recover to the electronic ground state non-radiatively. We draw this conclusion from the fact that no stimulated emission features (induced by one-photon absorption of the pump) are present in the TEA spectra for **ACyO** in both EtOH and DMSO, and that no emission was observed in the steady-state emission spectra of **ACyO** in both solvents when compared to blank scans of solvent-only solutions (spectra not shown). The lack of observed fluorescence would suggest that there is very poor Franck-Condon overlap between the S_1 minimum and the electronic ground state. These steady-state results further support our conclusion that the S_1/S_0 CI is accessed by >75% of **ACyO** molecules on ultrafast timescales as they are able to overcome the mild barrier from the S_1 minimum (0.04 eV) (Woolley et al., 2018).

For the **ACyO** population remaining in the excited state at extended time delays, >1.8 ns, it is likely that further repopulation of the electronic ground state and some photoproduct formation occurs. It is important to highlight that the systems we have studied are simple, isolated systems, therefore, we have observed repopulation of the electronic ground state at time beyond 1.8 ns. However, in a more complex environment like a sunscreen formulation, the population of **ACyO** in the S_1 excited state persisting beyond 1.8 ns has a greater chance of either forming a photoproduct or transferring that energy through collisions. This reinforces the importance of why an ideal UV filter would return to its electronic ground state on ultrafast timescales and why we conclude that **ACyO** is not a perfect UV filter candidate. We close the discussion by reiterating that more photoproduct formation appears to be occurring for **ACyO** in DMSO which is intuitively related to the lower GSB recovery quantum yield extracted from the TVA spectra presented above. The greater population persisting in the S_1 excited state at extended time delays, >1.8 ns, increases the probability for photoproduct formation.

CONCLUSION

Throughout the present work we have demonstrated that although **ACyO** has a long-lived excited state that persists

FIGURE 5 | UV/visible spectra of ~40 μM **ACyO** in **(A)** EtOH and **(B)** DMSO taken over varying durations of irradiation in a solar simulator. Black arrow on each plot denotes a decrease in absorbance at the absorption maxima after 7,200 s and corresponds to 2.0% for **ACyO** in EtOH and 6.5% for **ACyO** in DMSO.

beyond 2.5 ns, the extent of ground state recovery on ultrafast timescales is relatively high. We have determined that >75% of photoexcited **ACyO** in EtOH and DMSO is returning to its electronic ground state within 1.8 ns. These numbers appear to corroborate why **ACyO** displays good photostability in the isolated systems studied. Upon photoexcitation, we demonstrate that the majority of **ACyO** molecules have sufficient energy to overcome the S_1/S_0 CI barrier and relax non-radiatively on ultrafast timescales. Although **ACyO** displays long-lived features in accordance with previous studies (Losantos et al., 2017; Woolley et al., 2018), we propose that the cyclohexenone core is not as poor a UV filter as initially predicted, supporting nature's choice of the cyclohexenone core in MAAs. However, for an ideal UV filter we would ideally like as-close-to complete GSB recovery within ultrafast timescales; further studies on molecules with a cyclohexenone unit are therefore most-certainly warranted so as to provide clearer insight in to their photoprotective mechanisms, and how these mechanisms are influenced with substituent. In particular, how the GSB recovery quantum yield is influenced as we move progressively toward gadusol is one avenue to be explored, which could eventually guide the future design of UV filters based on MAAs.

In this present work, we have demonstrated that TVAS is a very powerful method when allied with appropriate high-level theory (in this case using explicit-solvent methodology which is important to consider when solute and solvent interact strongly with each other) for extracting accurate GSB recovery information. The combination of this high-level theory and TVAS enables vibrational ESA bands to be identified when selecting an integration region, allowing for the origins of a molecule's photostability to be traced. TVAS provides invaluable dynamical information that cannot be extracted from TEAS. Therefore, we suspect that this technique will see increasing use in the field of sunscreen science.

DATA AVAILABILITY STATEMENT

The datasets presented in this study can be found in online repositories. The names of the repository/repositories and accession number(s) can be found below: Zenodo repository doi: 10.5281/zenodo.3885450.

AUTHOR CONTRIBUTIONS

ALW conducted the majority of the experimental and computational work and took lead in writing the manuscript. MAPT ran the molecular dynamics simulations and provided support for the computational analysis. MAPT and JMW supervised the writing of the manuscript. DJLC and MDH helped conduct the transient vibrational absorption spectroscopy experiments presented in this paper. VGS conceived the experiment, supervised the writing of the manuscript, and supported the data analysis. All authors contributed to the article and approved the submitted version.

ACKNOWLEDGMENTS

SUPPLEMENTARY MATERIAL

The Supplementary Material for this article can be found online at: https://www.frontiersin.org/articles/10.3389/fchem.2020.574038/full#supplementary-material

REFERENCES

Adamo, C., and Barone, V. (1999). Toward reliable density functional methods without adjustable parameters: the PBE0 model. *J. Chem. Phys.* 110:6158. doi: 10.1063/1.478522

Arbeloa, E. M., Bertolotti, S. G., and Churio, M. S. (2011). Photophysics and reductive quenching reactivity of gadusol in solution. *Photochem. Photobiol. Sci.* 10, 133–142. doi: 10.1039/C0PP00250J

Baker, L. A., Horbury, M. D., Greenough, S. E., Allais, F., Walsh, P. S., Habershon, S., et al. (2016). Ultrafast photoprotecting sunscreens in natural plants. *J. Phys. Chem. Lett.* 7, 56–61. doi: 10.1021/acs.jpclett.5b02474

Baker, L. A., Horbury, M. D., Greenough, S. E., Coulter, P. M., Karsili, T. N. V., Roberts, G. M., et al. (2015). Probing the ultrafast energy dissipation mechanism of the sunscreen oxybenzone after UVA irradiation. *J. Phys. Chem. Lett.* 6, 1363–1368. doi: 10.1021/acs.jpclett.5b00417

Baker, L. A., Staniforth, M., Flourat, A. L., Allais, F., and Stavros, V. G. (2018). Gas-solution phase transient absorption study of the plant sunscreen derivative methyl sinapate. *ChemPhotoChem* 2, 743–748. doi: 10.1002/cptc.201800060

Balskus, E. P., and Walsh, C. T. (2010). The genetic and molecular basis for sunscreen biosynthesis in cyanobacteria. *Science* 329, 1653–1656. doi: 10.1126/science.1193637

Bandaranayake, W. M. (1998). Mycosporines: are they nature's sunscreens? *Nat. Prod. Rep.* 15, 159–172. doi: 10.1039/a815159y

Brenner, M., and Hearing, V. J. (2008). The protective role of melanin against UV damage in human skin. *Photochem. Photobiol.* 84, 539–549. doi: 10.1111/j.1751-1097.2007.00226.x

Bryden, A. M., Moseley, H., Ibbotson, S. H., Chowdhury, M. M., Beck, M. H., Bourke, J., et al. (2006). Photopatch testing of 1155 patients: results of the U.K. multicentre photopatch study group. *Br. J. Dermatol.* 155, 737–747. doi: 10.1111/j.1365-2133.2006.07458.x

Case, D. A., Berryman, J. T., Betz, R. M., Cerutti, D. S., Cheatham, T. E. III, Darden, T.A., et al. (2015). *AMBER 2015*. University of California: San Francisco, CA.

Casida, M. E. (1995). "Time-dependent density functional response theory for molecules," in *Recent Advances in Density Functional Methods,* ed D. P. Chong (Singapore: World Scientific), 155–192.

Conde, F. R., Churio, M. S., and Previtali, C. M. (2000). The photoprotector mechanism of mycosporine-like amino acids. Excited-state properties and photostability of porphyra-334 in aqueous solution. *J. Photochem. Photobiol. B Biol.* 56, 139–144. doi: 10.1016/S1011-1344(00)00066-X

Conde, F. R., Churio, M. S., and Previtali, C. M. (2007). Experimental study of the excited-state properties and photostability of the mycosporine-like amino acid palythine in aqueous solution. *Photochem. Photobiol. Sci.* 6, 669–674. doi: 10.1039/b618314j

Danovaro, R., Bongiorni, L., Corinaldesi, C., Giovannelli, D., Damiani, E., Astolfi, P., et al. (2008). Sunscreens cause coral bleaching by promoting viral infections. *Environ. Health Perspect.* 116, 441–447. doi: 10.1289/ehp.10966

Davidson, E. R. (1996). Comment on "comment on Dunning's correlation-consistent basis sets". *Chem. Phys. Lett.* 260, 514–518. doi: 10.1016/0009-2614(96)00917-7

Dean, J. C., Kusaka, R., Walsh, P. S., Allais, F., and Zwier, T. S. (2014). Plant sunscreens in the UV-B: ultraviolet spectroscopy of jet-cooled sinapoyl malate, sinapic acid, and sinapate ester derivatives. *J. Am. Chem. Soc.* 136, 14780–14795. doi: 10.1021/ja5059026

Downs, C. A., Kramarsky-Winter, E., Fauth, J. E., Segal, R., Bronstein, O., Jeger, R., et al. (2013). Toxicological effects of the sunscreen UV filter, benzophenone-2, on planulae and *in vitro* cells of the coral, stylophora pistillata. *Ecotoxicology* 23, 175–191. doi: 10.1007/s10646-013-1161-y

Downs, C. A., Kramarsky-Winter, E., Segal, R., Fauth, J., Knutson, S., Bronstein, O., et al. (2016). Toxicopathological effects of the sunscreen UV filter, oxybenzone (benzophenone-3), on coral planulae and cultured primary cells and its environmental contamination in Hawaii and the U.S. virgin Islands. *Arch. Environ. Contam. Toxicol.* 70, 265–288. doi: 10.1007/s00244-015-0227-7

Eller, M. S., and Gilchrest, B. A. (2000). Tanning as part of the eukaryotic SOS response. *Pigment Cell Res.* 13, 94–97. doi: 10.1034/j.1600-0749.13.s8.17.x

Gao, Q., and Garcia-Pichel, F. (2011). Microbial ultraviolet sunscreens. *Nat. Rev. Microbiol.* 9, 791–802. doi: 10.1038/nrmicro2649

Grieco, C., Kohl, F. R., Zhang, Y., Natarajan, S., Blancafort, L., and Kohler, B. (2018). Intermolecular hydrogen bonding modulates o-h photodissociation in molecular aggregates of a catechol derivative. *Photochem. Photobiol.* 95, 163–175. doi: 10.1111/php.13035

Grubb, M. P., Orr-Ewing, A. J., and Ashfold, M. N. R. (2014). KOALA: a program for the processing and decomposition of transient spectra. *Rev. Sci. Instrum.* 85:064104. doi: 10.1063/1.4884516

Hamm, P. (1995). Coherent effects in femtosecond infrared spectroscopy. *Chem. Phys.* 200, 415–429. doi: 10.1016/0301-0104(95)00262-6

Hatakeyama, M., Koizumi, K., Boero, M., Nobusada, K., Hori, H., Misonou, T., et al. (2019). Unique structural relaxations and molecular conformations of porphyra-334 at the excited state. *J. Phys. Chem. B* 123, 7649–7656. doi: 10.1021/acs.jpcb.9b03744

Holick, M. F. (2004). Sunlight and vitamin D for bone health and prevention of autoimmune diseases, cancers, and cardiovascular disease. *Am. J. Clin. Nutr.* 80, 1678s–1688s. doi: 10.1093/ajcn/80.6.1678S

Holm, A.-K., Rini, M., Nibbering, E. T. J., and Fidder, H. (2003). Femtosecond UV/mid-IR study of photochromism of the spiropyran 1′,3′-dihydro-1′,3′,3′-trimethyl-6-nitrospiro[2H-1-benzopyran-2,2′-(2H)-indole] in solution. *Chem. Phys. Lett.* 376, 214–219. doi: 10.1016/S0009-2614(03)00949-7

Horbury, M. D., Flourat, A. L., Greenough, S. E., Allais, F., and Stavros, V. G. (2018). Investigating isomer specific photoprotection in a model plant sunscreen. *ChemComm* 54, 936–939. doi: 10.1039/C7CC09061G

Horbury, M. D., Holt, E. L., Mouterde, L. M. M., Balaguer, P., Cebrián, J., Blasco, L., et al. (2019). Towards symmetry driven and nature inspired UV filter design. *Nat. Commun.* 10:4748. doi: 10.1038/s41467-019-12719-z

Horbury, M. D., Quan, W.-D., Flourat, A. L., Allais, F., and Stavros, V. G. (2017). Elucidating nuclear motions in a plant sunscreen during photoisomerization through solvent viscosity effects. *Phys. Chem. Chem. Phys.* 19, 21127–21131. doi: 10.1039/C7CP04070A

Humble, M. B. (2010). Vitamin D, light and mental health. *J. Photochem. Photobiol. B Biol.* 101, 142–149. doi: 10.1016/j.jphotobiol.2010.08.003

Klamt, A., and Schüürmann, G. (1993). COSMO: a new approach to dielectric screening in solvents with explicit expressions for the screening energy and its gradient. *J. Chem. Soc. Perkin. Trans.* 2, 799–805. doi: 10.1039/P29930000799

Koizumi, K., Hatakeyama, M., Boero, M., Nobusada, K., Hori, H., Misonou, T., et al. (2017). How seaweeds release the excess energy from sunlight to surrounding sea water. *Phys. Chem. Chem. Phys.* 19, 15745–15753. doi: 10.1039/C7CP02699D

Kollias, N., Sayre, R. M., Zeise, L., and Chedekel, M. R. (1991). New trends in photobiology; photoprotection by melanin. *J. Photochem. Photobiol. B* 9, 135–160. doi: 10.1016/1011-1344(91)80147-A

Losantos, R., Churio, M. S., and Sampedro, D. (2015). Computational exploration of the photoprotective potential of gadusol. *ChemistryOpen* 4, 155–160. doi: 10.1002/open.201402125

Losantos, R., Funes-Ardoiz, I., Aguilera, J., Herrera-Ceballos, E., Garcia-Iriepa, C., Campos, P. J., et al. (2017). Rational design and synthesis of efficient sunscreens to boost the solar protection factor. *Angew. Chem. Int. Ed.* 56, 2632–2635. doi: 10.1002/anie.201611627

Losantos, R., Lamas, I., Montero, R., Longarte, A., and Sampedro, D. (2019). Photophysical characterization of new and efficient synthetic sunscreens. *Phys. Chem. Chem. Phys.* 21, 11376–11384. doi: 10.1039/C9CP01267B

Lucas, R., McMichael, T., Smith, W., and Armstrong, B. (2006). "Solar ultraviolet radiation. global burden of disease from solar ultraviolet radiation," in *Environmental Burden of Disease Series, No. 13* eds. A. Prüss-Üstün, H. Zeeb, C. Mathers, and M. Repacholi (Geneva: World Health Organization), 1–87.

Luo, J., Liu, Y., Yang, S., Flourat, A. L., Allais, F., and Han, K. (2017). Ultrafast barrierless photoisomerization and strong ultraviolet absorption of photoproducts in plant sunscreens. *J. Phys. Chem. Lett.* 8, 1025–1030. doi: 10.1021/acs.jpclett.7b00083

Moliné, M., Arbeloa, E. M., Flores, M. R., Libkind, D., Farías, M. E., Bertolotti, S. G., et al. (2011). UVB photoprotective role of mycosporines in yeast: photostability and antioxidant activity of mycosporine-glutaminol-glucoside. *Radiat. Res.* 175, 44–50. doi: 10.1667/RR2245.1

Mullen, K. M., and Van Stokkum, I. H. M. (2007). TIMP: an R package for modeling multi-way spectroscopic measurements. *J. Stat. Softw.* 18, 1–46. doi: 10.18637/jss.v018.i03

Murdock, D., Harris, S. J., Clark, I. P., Greetham, G. M., Towrie, M., Orr-Ewing, A. J., et al. (2015). UV-induced isomerization dynamics of N-Methyl-2-pyridone in solution. *J. Phys. Chem. A* 119, 88–94. doi: 10.1021/jp511818k

Murdock, D., Harris, S. J., Luke, J., Grubb, M. P., Orr-Ewing, A. J., and Ashfold, M. N. R. (2014). Transient UV pump–IR probe investigation of heterocyclic ring-opening dynamics in the solution phase: the role played by no* states in the photoinduced reactions of thiophenone and furanone. *Phys. Chem. Chem. Phys.* 16, 21271–21279. doi: 10.1039/C4CP03653K

Nibbering, E. T. J., Fidder, H., and Pines, E. (2005). ULTRAFAST CHEMISTRY: using time-resolved vibrational spectroscopy for interrogation of structural dynamics. *Annu. Rev. Phys. Chem.* 56, 337–367. doi: 10.1146/annurev.physchem.56.092503.141314

Perdew, J. P., Ernzerhof, M., and Burke, K. (1996). Rationale for mixing exact exchange with density functional approximations. *J. Chem. Phys.* 105, 9982–9985. doi: 10.1063/1.472933

Rastogi, R. P., and Incharoensakdi, A. (2014). UV radiation-induced biosynthesis, stability and antioxidant activity of mycosporine-like amino acids (MAAs) in a unicellular cyanobacterium gloeocapsa sp. CU2556. *J. Photochem. Photobiol. B Biol.* 130, 287–292. doi: 10.1016/j.jphotobiol.2013.12.001

Rini, M., Holm, A.-K., Nibbering, E. T. J., and Fidder, H. (2003). Ultrafast UV-mid-IR investigation of the ring opening reaction of a photochromic spiropyran. *J. Am. Chem. Soc.* 125, 3028–3034. doi: 10.1021/ja028262j

Sampedro, D. (2011). Computational exploration of natural sunscreens. *Phys. Chem. Chem. Phys.* 13, 5584–5586. doi: 10.1039/c0cp02901g

Schaap, I., and Slijkerman, D. M. E. (2018). An environmental risk assessment of three organic UV-filters at lac bay, bonaire, southern caribbean. *Mar. Pollut. Bull.* 135, 490–495. doi: 10.1016/j.marpolbul.2018.07.054

Sinha, R. P., Klisch, M., Gröniger, A., and Häder, D.-P. (2000). Mycosporine-like amino acids in the marine red alga gracilaria cornea - effects of UV and heat. *Environ. Exp. Bot.* 43, 33–43. doi: 10.1016/S0098-8472(99)00043-X

Sinha, R. P., Singh, S. P., and Hader, D. P. (2007). Database on mycosporines and mycosporine-like amino acids (MAAs) in fungi, cyanobacteria, macroalgae, phytoplankton and animals. *J. Photochem. Photobiol. B Biol.* 89, 29–35. doi: 10.1016/j.jphotobiol.2007.07.006

Snellenburg, J. J., Laptenok, S., Seger, R., Mullen, K. M., and Van Stokkum, I. H. M. (2012). Glotaran: a java-based graphical user interface for the R package TIMP. *J. Stat. Softw.* 49, 1–22. doi: 10.18637/jss.v049.i03

Sui, X.-X., Li, L., Zhao, Y., Wang, H.-G., Pei, K.-M., and Zheng, X. (2012). Resonance raman and density functional study of the excited state structural dynamics of 3-amino-2-cyclohexen-1-one in water and acetonitrile solvents. *Spectrochim. Acta A* 85, 165–172. doi: 10.1016/j.saa.2011.09.055

Turner, M. A. P., Turner, R. J., Horbury, M. D., Hine, N. D. M., and Stavros, V. G. (2019). Examining solvent effects on the ultrafast dynamics of catechol. *J. Chem. Phys.* 151:084305. doi: 10.1063/1.5116312

Valiev, M., Bylaska, E. J., Govind, N., Kowalski, K., Straatsma, T. P., Van Dam, H. J. J., et al. (2010). NWChem: a comprehensive and scalable open-source solution for large scale molecular simulations. *Comput. Phys. Commun.* 181, 1477–1489. doi: 10.1016/j.cpc.2010.04.018

Wang, S. Q., and Lim, H. W. (2016). *Principles and Practice of Photoprotection.* Switzerland: ADIS.

Warshaw, E. M., Wang, M. Z., Maibach, H. I., Belsito, D. V., Zug, K. A., Taylor, J. S., et al. (2013). Patch test reactions associated with sunscreen products and the importance of testing to an expanded series: retrospective analysis of North American contact dermatitis group data, 2001 to 2010. *Dermatitis* 24, 176–182. doi: 10.1097/DER.0b013e3182983845

White, J. D., Cammack, J. H., and Sakuma, K. (1989). The synthesis and absolute configuration of mycosporins. A novel application of the Staudinger reaction. *J. Am. Chem. Soc.* 111, 8970–8972. doi: 10.1021/ja00206a059

White, J. D., Cammack, J. H., Sakuma, K., Rewcastle, G. W., and Widener, R. K. (1995). Transformations of quinic acid. Asymmetric synthesis and absolute configuration of mycosporin i and mycosporin-gly. *J. Org. Chem.* 60, 3600–3611. doi: 10.1021/jo00117a008

Winget, P., Dolney, D. M., Giesen, D. J., Cramer, C. J., and Truhlar, D. G. (1999). *Minnesota Solvent Descriptor Database.* Minneapolis, MN: Department of Chemistry and Supercomputer Institute; University of Minnesota.

Woolley, J. M., Staniforth, M., Horbury, M. D., Richings, G. W., Wills, M., and Stavros, V. G. (2018). Unravelling the photoprotection properties of mycosporine amino acid motifs. *J. Phys. Chem. Lett.* 9, 3043–3048. doi: 10.1021/acs.jpclett.8b00921

York, D. M., and Karplus, M. (1999). A smooth solvation potential based on the conductor-like screening model. *J. Phys. Chem. A* 103, 11060–11079. doi: 10.1021/jp992097l

Zhao, X., Luo, J., Liu, Y., Pandey, P., Yang, S., Wei, D., et al. (2019a). Substitution dependent ultrafast ultraviolet energy dissipation mechanisms of plant sunscreens. *J. Phys. Chem. Lett.* 10, 5244–5249. doi: 10.1021/acs.jpclett.9b02175

Zhao, X., Luo, J., Yang, S., and Han, K. (2019b). New insight into the photoprotection mechanism of plant sunscreens: adiabatic relaxation competing with nonadiabatic relaxation in the cis → trans photoisomerization of methyl sinapate. *J. Phys. Chem. Lett.* 10, 4197–4202. doi: 10.1021/acs.jpclett.9b01651

Zuehlsdorff, T. J., Haynes, P. D., Payne, M. C., and Hine, N. D. M. (2017). Predicting solvatochromic shifts and colours of a solvated organic dye: The example of nile red. *J. Chem. Phys.* 146:124504. doi: 10.1063/1.4979196